Research paper

Modelling uncertainties in phase-space boundary integral models of ray propagation

Janis Bajars [a], David J. Chappell [b],*

[a] *Faculty of Physics, Mathematics and Optometry, University of Latvia, Jelgavas Street, Riga, LV-1004, Latvia*
[b] *School of Science and Technology, Nottingham Trent University, Clifton Campus, Nottingham NG11 8NS, UK*

A R T I C L E   I N F O

A B S T R A C T

A recently proposed phase-space boundary integral model for the stochastic propagation of ray densities is presented and, for the first time, explicit connections between this model and parametric uncertainties arising in the underlying physical model are derived. In particular, an asymptotic analysis for a weak noise perturbation of the propagation speed is used to derive expressions for the probability distribution of the phase-space boundary coordinates after transport along uncertain, and in general curved, ray trajectories. Furthermore, models are presented for incorporating geometric uncertainties in terms of both the location of an edge within a polygonal domain, as well as small scale geometric fluctuations giving rise to rough boundary reflections. Uncertain source terms are also considered in the form of stochastically distributed point sources and uncertain boundary data. A series of numerical experiments is then performed to illustrate these uncertainty models in two-dimensional convex polygonal domains.

1. Introduction

Modelling ray propagation in uncertain domains $\Omega \subset \mathbb{R}^d$, through uncertain media or resulting from uncertain source terms is important for a wealth of applications in high-frequency wave modelling; application areas include optics, acoustics, seismology, structural mechanics and electromagnetics. In this paper we consider stochastically smoothed transfer operators [1–4] as the foundation of a model to describe these uncertainties. These operators can be applied to describe the stochastic evolution of a density along a non-interacting particle (or ray) trajectory flow, where both the arrival location of the particle and its boundary reflections are uncertain. The corresponding deterministic particle flow with specular boundary reflections is typically used to describe the mean behaviour of the stochastic particle evolution and in the case $d = 2$ considered here, these deterministic flow problems are often termed dynamical billiards [5].

Stochastic transfer operator models arise when considering the evolution of a probability density distribution ρ in phase-space $\mathbb{R}^{2d}$ under the action of a stochastic dynamical system of the form [6]

$$\mathrm{d}X = \mathbf{V}(X)\mathrm{d}t + \sigma \,\mathrm{d}W, \tag{1}$$

* Corresponding author.
E-mail address: david.chappell@ntu.ac.uk (D.J. Chappell).

where $\sigma > 0$ and W is a $2d$-dimensional Wiener process. The solutions X are time-dependent random variables such that

$$\text{Prob}(X(t) \in A) = \int_A \rho(Y, t) \, dY.$$

The density ρ may then be characterized by the Fokker–Planck equation

$$\frac{\partial \rho}{\partial t} + \nabla \cdot (\mathbf{V} \rho) = \frac{\sigma^2}{2} \Delta \rho, \tag{2}$$

provided that the vector field $\mathbf{V}$ is sufficiently smooth. The solution of this equation may be represented using the following Wiener integral [7], sometimes known as the Fokker–Planck operator [3]

$$\mathcal{L}^t[\rho](X) = \frac{1}{(2\pi\sigma^2 \delta t)^d} \int_{\mathbb{R}^{2d}} \exp\left(-\int_0^t \frac{[\dot{X}(\tau) - \mathbf{V}(X(\tau))]^2}{2\sigma^2} \, d\tau \right) \rho(X, 0) \, dX(t) \tag{3}$$

in the limit where the time increment $\delta t \to 0$. We sidestep the proper definition of $\dot{X}$ and the formal limit as $\delta t \to 0$ here since we will soon abandon the above continuous dynamical system form of the model for a reformulation in terms of discrete flow maps, and consequently neither issue will be of concern.

Since the late nineties, stochastic transfer operators have predominantly been studied using periodic orbit techniques [1,8–11]. More recently, higher dimensional flows [3] and the estimation of stationary distributions [12] have also been considered. The discretisation of (deterministic) transfer operator based models for the evolution of phase-space densities has traditionally been performed using the Ulam method [13], whereby a cellular subdivision of phase-space is applied and local approximations of the cell-to-cell transition rates are then calculated. However, it was some years later until these methods were applied specifically to stochastic transfer operators, for example Refs. [6,14]. More recent work has focussed on perturbation theory for the evaluation of long-time observables [15] and to quantify uncertainties [16]. The present work continues along this direction by considering perturbation techniques for the modelling of parametric uncertainties in the weak noise regime.

In this work we restrict our attention to the case when $\mathbf{V}$ describes a Hamiltonian system and denote the associated Hamiltonian H. In particular, we consider stationary solutions ρ_∞ of the Fokker–Planck equation:

$$\{\rho_\infty, H\} = \frac{\sigma^2}{2} \Delta \rho_\infty. \tag{4}$$

This model includes approximations to frequency domain high-frequency wave problems as a notable special case [17]. We note that (4) provides a tractable model for the stationary problem in bounded domains [17], since it circumvents the need to directly evaluate the long-time dynamics in terms of multiple reflections of rays (potentially leading an exponentially increasing number of trajectories to track); methods whereby trajectories (or swarms of trajectories) are directly tracked through phase-space are usually termed *ray tracing* [18]. The incorporation of uncertainties in ray tracing models has previously been considered for modelling high intensity focussed ultrasound [19] and rough surface reflections [20] in acoustics, for modelling electromagnetic high-frequency wave problems using a polynomial chaos approach [21] and for modelling current driven plasma waves using a combined ray tracing and Fokker–Planck model [22].

Long-time stochastic dynamics in high-frequency wave problems may also be considered in terms of non-parametric uncertainty models; this type of model can even be applied without any knowledge relating to the specific nature of the uncertainties present in the system. Statistical Energy Analysis (SEA) is perhaps the most well-known approach of this type for modelling high-frequency noise and vibrations, see for example Refs. [23] and [24]. To construct an SEA model, one divides a structure into a set of subsystems and then ergodicity of the underlying ray dynamics as well as quasi-equilibrium conditions are postulated. The advantage is that one obtains a simplified and relatively small linear system to solve, based only on coupling constants between subsystems. However, the particular sub-division of the structure is critical to the validity of the underlying assumptions, which are often hard to verify. We note that more sophisticated non-parametric uncertainty models have also been developed using random matrix theory to gain improved statistical models for applications in both vibro-acoustics [25] and electromagnetics [26].

In what follows, we concentrate on stochastic ray-based models for linear wave problems that incorporate uncertainties in the ray dynamics via stochastic evolution operators. In particular, we consider a reformulation of the Fokker–Planck operator (3) for evolving a discrete map φ and replace σ by a vector $\boldsymbol{\sigma}$ prescribing different rates of diffusion in position and momentum space. The iterates of the map φ are equivalent to a discrete time sampling of the trajectory flow $X(t)$ at times when X is located on the boundary of a bounded domain $\Omega \subset \mathbb{R}^2$. In this study we derive, for the first time, the explicit connections between the above described stochastic evolution operator model for the propagation of a ray density via uncertain ray dynamics and small parametric uncertainties in various aspects of the physical model, including the source location, the geometry, the surface roughness and the propagation speed. Most significantly, in the latter case we give a detailed asymptotic analysis to describe the distribution of the phase-space coordinate on the boundary of Ω after transport through an uncertain material or substance within Ω.

The paper is structured as follows: in Section 2 we will outline a boundary integral model for the stochastic evolution of phase-space densities through bounded domains $\Omega \subset \mathbb{R}^2$. In Section 3 we will then detail the incorporation of specific model uncertainties using the framework presented in Section 2. In particular, we will consider weak noise material parametric
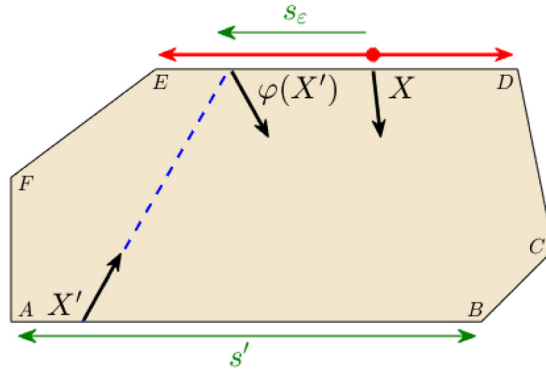
Fig. 1. Ray trajectories given by a noisy boundary map inside a convex polygon $\Omega = ABCDEF$.

uncertainties in Section 3.1, geometric uncertainties in Section 3.2 and uncertain source terms in Section 3.3. The numerical implementation of the boundary integral model from Section 2 will be described in Section 4.1, before presenting a series of numerical examples in Section 4.2, in order to illustrate the uncertainty models from Section 3.

2. A stochastic boundary integral model for propagating densities

In this section we present an overview of the problem set-up, for more details see Ref. [27]. Consider a Hamiltonian system governed by

$$\hat{H}(\mathbf{r}, \mathbf{p}) = c(\mathbf{r})|\mathbf{p}| \equiv 1,$$

which describes trajectories propagating at speed c between reflections at the boundary $\Gamma = \partial\Omega$; these trajectories are simply straight line paths when c is a constant. The phase-space coordinates $(\mathbf{r}, \mathbf{p})$ denote the position $\mathbf{r} \in \Omega \subset \mathbb{R}^2$ and the momentum or slowness vector $\mathbf{p} \in \mathbb{R}^2$, respectively. Furthermore, we denote the Birkhoff coordinates on the boundary Γ as $X = (s, p)$. Here, the first coordinate s is an arc-length coordinate for the position on Γ and the second, $p = c^{-1}\sin(\theta)$, is the tangential component of the slowness $\mathbf{p}$ at the point s. The angle $\theta \in (-\pi/2, \pi/2)$ is formed between the normal vector to Γ and the trajectory leaving the boundary at the point s. For simplicity, we limit our discussion to convex polygonal domains Ω in order to avoid the additional complexities involved in implementing visibility functions or curved boundary segments.

A reformulation of the Fokker–Planck operator (3) for propagating a phase-space density ρ through Ω from a starting point $s' \in \Gamma$, until reaching another point $s \in \Gamma$, is given as follows [4,27]

$$\mathcal{L}_{\boldsymbol{\sigma}}\rho(X) = \int_Q f_{\boldsymbol{\sigma}}(X - \varphi(X'))\rho(X')\,\mathrm{d}X'. \tag{5}$$

The integral in Eq. (5) is over the boundary phase-space $Q = \Gamma \times (-c^{-1}, c^{-1})$ and $\varphi: Q \to Q$ denotes the (deterministic) boundary map mentioned above, which may be written in component form as

$$\varphi(X') = (\varphi_s(X'), \varphi_p(X')). \tag{6}$$

Here $X' = (s', p') \in Q$ and the map φ therefore corresponds to a translation from s' to $\varphi_s(X')$, together with a rotation equivalent to a specular reflection at $\varphi_s(X')$ (denoted $\varphi_p(X')$) as shown in Fig. 1. The function $f_{\boldsymbol{\sigma}}$ appearing in (5) is a probability density function (PDF) satisfying

$$\int_Q f_{\boldsymbol{\sigma}}(X - \varphi(X'))\,\mathrm{d}X = 1, \tag{7}$$

where $\boldsymbol{\sigma}$ is a parameter set related to the spread of the distribution.

The PDF $f_{\boldsymbol{\sigma}}$ may be chosen according to the requirements of a given application and will be discussed further in the next section. However, note that the boundary map φ has finite range (in both variables) and so it is natural to consider only PDFs with finite support. This differs from the models based on the Fokker–Planck operator (3) described in the introduction. The density evolution described by the operator (5) corresponds to a stochastic boundary map $\varphi_{\boldsymbol{\sigma}}(X') = \varphi(X') + X_\varepsilon$ with additive noise $X_\varepsilon = (s_\varepsilon, p_\varepsilon)$ where the random variables $(s_\varepsilon, p_\varepsilon)$ are drawn from the PDF $f_{\boldsymbol{\sigma}}$. Rearranging to obtain the deterministic boundary map $\varphi(X') = X - X_\varepsilon$ for given $\varphi_{\boldsymbol{\sigma}}(X') = X \in Q$, then the domain of $f_{\boldsymbol{\sigma}}$ (that is, the admissible values of X_ε) should be restricted so that the values $X - X_\varepsilon$ are within the range of φ. We denote the support of $f_{\boldsymbol{\sigma}}$ by (X^-, X^+) for $X^\pm = (s^\pm, p^\pm)$. A relatively straightforward calculation then gives $p^\pm = \pm c^{-1} - \varphi_p(X')$.

The stationary density ρ_∞ is defined by the Neumann series

$$\rho_\infty = \sum_{j=0}^\infty (\mathcal{L}_{\boldsymbol{\sigma}})^{(j)}\rho_0, \tag{8}$$
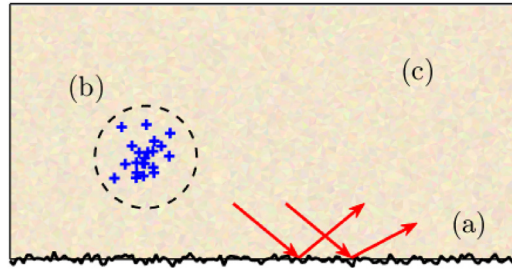
Fig. 2. Parametric uncertainties illustrated on a rectangular domain showing (a) uncertain geometry, (b) uncertain source terms and (c) uncertain material parameters.

where the sum to infinity includes contributions from arbitrarily many reflections. In particular, the superscript (j) denotes the jth iteration of the operator $\mathcal{L}_\sigma$ acting on an initial boundary density ρ_0, and each iterate corresponds to a reflection from or transmission through Γ. The series (8) will only converge if energy losses have been included in the model. These losses could arise, for example, from structural damping or from reflections at partially absorbing boundaries. In this work we introduce a damping term of the form $\exp(-\mu d(s, s'))$, which corresponds to a structural damping model with damping coefficient $\mu \geq 0$ and where $d(s, s')$ is the Euclidean distance between the trajectory endpoints s' and s on Γ. Provided that the Neumann series (8) converges, then we obtain a second-kind Fredholm boundary integral equation [4,27]

$$(I - \mathcal{L}_\sigma)\rho_\infty = \rho_0 \tag{9}$$

for ρ_∞.

Once the stationary boundary density ρ_∞ has been calculated using Eq. (9), it may then be projected into the interior of Ω to give the corresponding interior stationary density ρ_Ω. For a constant speed of propagation c, ρ_Ω may be evaluated at a point $\mathbf{r} \in \Omega$ as (see for example Ref. [17])

$$\rho_\Omega(\mathbf{r}) = \frac{1}{c^2} \int_\Gamma \frac{\cos(\vartheta(\mathbf{r}_s, \mathbf{r})) \exp(-\mu|\mathbf{r} - \mathbf{r}_s|)}{|\mathbf{r} - \mathbf{r}_s|} \rho_\infty(s, p) \, ds. \tag{10}$$

Here, $\mathbf{r}_s$ represents the Cartesian coordinates corresponding to $s \in \Gamma$ and $\vartheta(\mathbf{r}_s, \mathbf{r})$ is the angle between the trajectory direction vector $\mathbf{r} - \mathbf{r}_s$ and the normal vector to Γ at s.

3. Uncertainty modelling

In this section we model three distinct sources of uncertainty, as illustrated in Fig. 2, within the stochastic boundary integral operator framework introduced above. In particular, we explain how the PDF f_σ can be chosen in order to model different types of uncertainty arising in a particular application.

3.1. Uncertain material parameters

In this work we consider a simple model where the material inside the domain Ω is characterised by a single parameter c, the propagation speed. However, we note that such a model includes within it the potential to model a wide range of parameter uncertainties upon which c depends for different applications, for example, temperature, density, Young's modulus and so on. In this section we perform an asymptotic analysis to predict the distribution of trajectories arising from a small uncertainty in c of the form

$$c(\mathbf{r}) = c_0 + \boldsymbol{\epsilon} \cdot \bar{\mathbf{c}}(\mathbf{r}). \tag{11}$$

Here $\mathbf{r} = (r_x, r_y)^T$ is the trajectory position, $c_0 > 0$ is the mean propagation speed and $|\boldsymbol{\epsilon}| \ll c_0$, $\boldsymbol{\epsilon} = (\epsilon_x, \epsilon_y)^T$, where $\epsilon_x, \epsilon_y \sim \mathcal{N}(0, \sigma_c^2)$ are normally distributed random variables with mean 0 and variance σ_c^2. The normal distribution is a popular choice for modelling noise and is appropriate here under the assumptions that c is equally likely to be either greater or less than c_0 and is more likely to be in the vicinity of c_0 than further away [28]. However, we note that the subsequent asymptotic analysis is not limited to the normal distribution, rather it is limited to a weak noise perturbation about the mean. The vector valued function $\bar{\mathbf{c}} : \Omega \to \mathbb{R}^2$ is assumed to define a continuously differentiable (in both variables) perturbation of the propagation speed in the bounded domain Ω. We note that our methods allow for fairly general choices of $\bar{\mathbf{c}}$, but also that the coefficients of the asymptotic series will depend on this choice and so one should consider whether it will adversely affect their convergence.

3.1.1. Asymptotic approximation of the trajectory deformation

The stochastic perturbation in c (11) means that instead of straight-line trajectories, the Hamiltonian $\hat{H} = c|\mathbf{p}| = 1$ here describes curved propagation paths in general, which are governed by the dynamical system

$$\dot{\mathbf{r}} = c(\mathbf{r})^2 \mathbf{p},$$

$$c(\boldsymbol{r})\dot{\boldsymbol{p}} = -\nabla c(\boldsymbol{r}), \tag{12}$$

with initial conditions $\boldsymbol{r}(0) = \boldsymbol{r}_0$ and $\boldsymbol{p}(0) = \boldsymbol{p}_0/c_0$ for $|\boldsymbol{p}_0| = 1$. We seek a solution of (12) with propagation speed given by (11) in the form of the asymptotic expansions:

$$\boldsymbol{r}(t) = \boldsymbol{r}_0 + c_0 \boldsymbol{p}_0 t + \bar{\boldsymbol{R}}(t)\boldsymbol{\epsilon} + \dots,$$
$$\boldsymbol{p}(t) = \frac{1}{c_0}\boldsymbol{p}_0 + \bar{\boldsymbol{P}}(t)\boldsymbol{\epsilon} + \dots, \tag{13}$$

where $\bar{\boldsymbol{R}} : \mathbb{R}_+ \to \mathbb{R}^{2\times2}$ and $\bar{\boldsymbol{P}} : \mathbb{R}_+ \to \mathbb{R}^{2\times2}$ are unknown matrix perturbation functions. In general, we consider the asymptotic expansions (13) up to first order in $\boldsymbol{\epsilon}$ only, that is, we are seeking only the first order correction to the straight-line trajectory solution when $\boldsymbol{\epsilon} = \boldsymbol{0}$. We will see later that this is sufficient to derive closed form expressions for the PDFs for the each of the boundary phase-space trajectory coordinates when using a model based on the normal distribution. It may be necessary to include higher order terms for other choices of distribution. Combining (13) with the expression for the propagation speed (11) and substituting into the system (12) leads to the following system of matrix differential equations for the perturbation functions $\bar{\boldsymbol{R}}$ and $\bar{\boldsymbol{P}}$:

$$\dot{\bar{\boldsymbol{R}}}(t) = 2\boldsymbol{p}_0 \otimes \bar{\boldsymbol{c}}(\boldsymbol{r}_0 + c_0 \boldsymbol{p}_0 t) + c_0^2 \bar{\boldsymbol{P}}(t),$$
$$c_0 \dot{\bar{\boldsymbol{P}}}(t) = -\nabla \bar{\boldsymbol{c}}(\boldsymbol{r}_0 + c_0 \boldsymbol{p}_0 t), \tag{14}$$

where $\otimes$ denotes the Kronecker product. Since the second equation is independent of $\bar{\boldsymbol{R}}(t)$, the solution to the system (14) can be calculated directly from the integrals

$$\bar{\boldsymbol{R}}(t) = \int_0^t \left(2\boldsymbol{p}_0 \otimes \bar{\boldsymbol{c}}(\boldsymbol{r}_0 + c_0 \boldsymbol{p}_0 \tau) + c_0^2 \bar{\boldsymbol{P}}(\tau) \right) d\tau,$$
$$\bar{\boldsymbol{P}}(t) = -\frac{1}{c_0} \int_0^t \nabla \bar{\boldsymbol{c}}(\boldsymbol{r}_0 + c_0 \boldsymbol{p}_0 \tau) \, d\tau. \tag{15}$$

3.1.2. Verification of the asymptotic approximation

For simplicity, we will consider the case when the perturbation function $\bar{\boldsymbol{c}}(\boldsymbol{r})$ is linear and set

$$c(\boldsymbol{r}) = c_0 + \boldsymbol{\epsilon} \cdot (\boldsymbol{r} - \boldsymbol{r}_0). \tag{16}$$

We note that the asymptotic analysis described above holds more generally, but this special case proves useful as a test case since the asymptotic approximation (13) simplifies to

$$\boldsymbol{r}(t) = \boldsymbol{r}_0 + c_0 \boldsymbol{p}_0 t + \frac{c_0}{2}(2(\boldsymbol{p}_0 \otimes \boldsymbol{p}_0) - \mathrm{I})\boldsymbol{\epsilon} t^2 + \frac{c_0}{12}\left(\boldsymbol{\epsilon}^T \tilde{\boldsymbol{R}}_x \boldsymbol{\epsilon}, \boldsymbol{\epsilon}^T \tilde{\boldsymbol{R}}_y \boldsymbol{\epsilon} \right)^T t^3 + \dots,$$
$$\boldsymbol{p}(t) = \frac{1}{c_0}\boldsymbol{p}_0 - \frac{1}{c_0}\boldsymbol{\epsilon} t + \frac{1}{4c_0}\left(\boldsymbol{\epsilon}^T \tilde{\boldsymbol{P}}_x \boldsymbol{\epsilon}, \boldsymbol{\epsilon}^T \tilde{\boldsymbol{P}}_y \boldsymbol{\epsilon} \right)^T t^2 + \dots, \tag{17}$$

where we have also included second order terms for the purposes of analysis in Section 3.1.3. The perturbation matrices are given by

$$\tilde{\boldsymbol{R}}_x = \begin{pmatrix} -10p_{x0} + 12p_{x0}^3 - 3p_{y0} + 12p_{x0}^2 p_{y0} \\ -3p_{y0} + 12p_{x0}^2 p_{y0} - 4p_{x0} + 12p_{x0}p_{y0}^2 \end{pmatrix},$$

$$\tilde{\boldsymbol{R}}_y = \begin{pmatrix} -4p_{y0} + 12p_{x0}^2 p_{y0} - 3p_{x0} + 12p_{x0}p_{y0}^2 \\ -3p_{x0} + 12p_{x0}p_{y0}^2 - 10p_{y0} + 12p_{y0}^3 \end{pmatrix},$$

$$\tilde{\boldsymbol{P}}_x = \begin{pmatrix} 2p_{x0} & p_{y0} \\ p_{y0} & 0 \end{pmatrix} \quad \text{and} \quad \tilde{\boldsymbol{P}}_y = \begin{pmatrix} 0 & p_{x0} \\ p_{x0} & 2p_{y0} \end{pmatrix},$$

where p_{x0} and p_{y0} refer to the entries of the initial unit momentum vector $\boldsymbol{p}_0 = (p_{x0}, p_{y0})^T$. In addition, we note that the choice of a linear perturbation (16) leads to rotational invariance of the solution. One can see this by considering $\hat{\boldsymbol{r}} = R_\phi \boldsymbol{r}$, where R_ϕ is the standard rotation matrix giving an anti-clockwise rotation through the angle ϕ in two-dimensional Euclidean space. It is straightforward to show that $c(\boldsymbol{r} + \boldsymbol{r}_0) = c_0 + \boldsymbol{\epsilon} \cdot \boldsymbol{r} = c_0 + \hat{\boldsymbol{\epsilon}} \cdot \hat{\boldsymbol{r}}$, with c given by (16). Since in this case we also have that $\nabla c = \boldsymbol{\epsilon}$, then it follows that the dynamical system (12) is invariant under the action of R_ϕ.

An exact solution to the dynamical system (12) with linear propagation speed (16) can also be derived in the special case when $\boldsymbol{\epsilon} := \epsilon_x = \epsilon_y$. This analytical solution is detailed in Appendix A; we use it here to verify our asymptotic approximation (17) as shown in Fig. 3. The plot shows trajectories computed for three different values of $\boldsymbol{\epsilon}$ with $c_0 = 1$ and the initial conditions $\boldsymbol{r}_0 = \boldsymbol{0}$ and $\boldsymbol{p}_0 = (1, 0)^T$. The solutions are computed until the trajectory intersects the line $r_x = 1$. The plot shows good agreement between the analytical and (first and second order) asymptotic solutions. As expected, the match is better for the second order asymptotic approximation, for smaller choices of $\boldsymbol{\epsilon}$ or if shorter trajectories are considered.
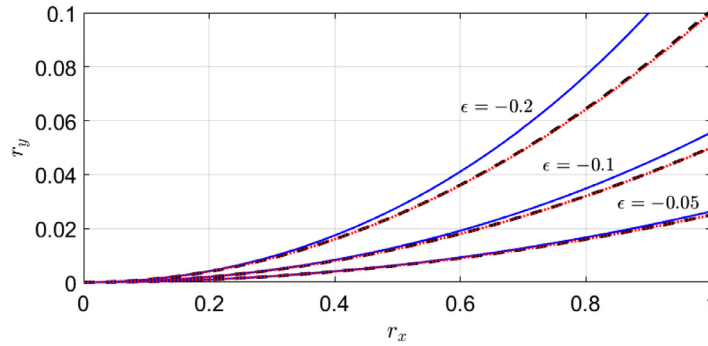
Fig. 3. Comparison between analytical (dashed), first order asymptotic (solid) and second order asymptotic (dotted) trajectory solutions $\mathbf{r} = (r_x, r_y)$ of the system (12) for a linear propagation speed function (16) with different values of $\boldsymbol{\epsilon} = (\epsilon_x, \epsilon_y)$ such that $\epsilon_x = \epsilon_y = \epsilon$. Initial conditions and parameter values: $\mathbf{r}_0 = \mathbf{0}$, $\mathbf{p}_0 = (1, 0)^T$ and $c_0 = 1$.

3.1.3. Statistics of the noisy boundary flow map

We now consider the statistical properties of the trajectories governed by the asymptotic solution (17) when $\epsilon_x, \epsilon_y \sim \mathcal{N}(0, \sigma_c^2)$, again noting that other probability distributions could be used to model the weak additive noise. In particular, we study the distribution of arrival positions at a straight-line receiving boundary as a probability distribution whose mean corresponds to the straight line trajectory produced when $\epsilon_x = \epsilon_y = 0$. The consequence of the rotational invariance described above is that the distribution of arrival positions depends only on the direction of the initial unit momentum vector $\mathbf{p}_0$ relative to the orientation of the receiving boundary, rather than depending on each of these independently. We therefore restrict to studying the distribution of arrival positions on a boundary line parallel to the y-axis given by $r_x = L$, with $L > 0$ a constant, for different values of the initial unit momentum vector $\mathbf{p}_0$ and a fixed initial position $\mathbf{r}_0 = \mathbf{0}$. We will consider the dependence of the distribution of $r_y(t)$ on the probability distribution from which $\boldsymbol{\epsilon}$ is sampled at the time $t = t^*$ where $r_x(t^*) = L$.

Let us take $\mathbf{p}_0 = (\cos(\theta'), \sin(\theta'))^T$, where $\theta' \in (-\pi/2, \pi/2)$ is the angle between the normal vector $((1, 0)^T$ in our example) and the trajectory, evaluated at its initial point. Then we consider the asymptotic solution (17) and note that fixing $r_x(t^*) = L$ leads to the following equation for the arrival time t^*:

$$L = c_0 \cos(\theta') t^* + \frac{c_0}{2} \left(\cos(2\theta') \epsilon_x + \sin(2\theta') \epsilon_y \right) t^{*2} + \frac{c_0}{6} \left((-5 \cos(\theta') + 6 \cos^3(\theta')) \epsilon_x^2 \right.$$
$$\left. + (12 \cos^2(\theta') \sin(\theta') - 3 \sin(\theta')) \epsilon_x \epsilon_y + (6 \cos(\theta') \sin^2(\theta') - 2 \cos(\theta')) \epsilon_y^2 \right) t^{*3} + \dots$$

To find t^* we consider the asymptotic expansion

$$t^* = t_0 + t_x \epsilon_x + t_y \epsilon_y + t_{xx} \epsilon_x^2 + t_{xy} \epsilon_x \epsilon_y + t_{yy} \epsilon_y^2 + \dots \tag{18}$$
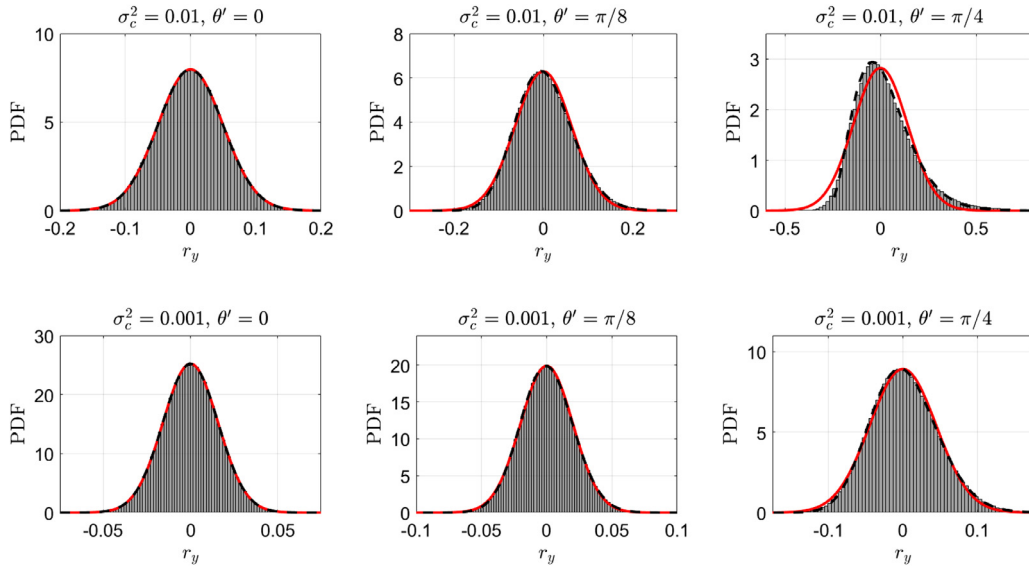
and find that the expansion coefficients are

$$t_0 = \frac{L}{c_0} \sec(\theta'), \quad t_x = -\frac{L^2}{2c_0^2} \cos(2\theta') \sec^3(\theta'), \quad t_y = -\frac{L^2}{c_0^2} \tan(\theta') \sec(\theta'),$$

$$t_{xx} = \frac{L^3}{6c_0^3} (6 \cos^4(\theta') - 7 \cos^2(\theta') + 3) \sec^5(\theta'),$$

$$t_{xy} = \frac{L^3}{2c_0^3} \tan(\theta') (4 \cos^2(\theta') - 3) \sec^3(\theta'),$$

$$t_{yy} = -\frac{L^3}{3c_0^3} (3 \cos^2(\theta') - 4) \sec^3(\theta').$$

The solution r_y may then be computed at $t = t^*$ using (17) as follows

$$r_y(\boldsymbol{\epsilon}, \theta') = L \tan(\theta') + \frac{L^2}{2c_0} \tan(\theta') \sec^2(\theta') \epsilon_x - \frac{L^2}{2c_0} \sec^2(\theta') \epsilon_y$$

$$+ \frac{L^3}{2c_0^2} \tan^3(\theta') \sec^2(\theta') \epsilon_x^2 - \frac{L^3}{c_0^2} \tan^2(\theta') \sec^2(\theta') \epsilon_x \epsilon_y$$

$$+ \frac{L^3}{2c_0^2} \tan(\theta') \sec^2(\theta') \epsilon_y^2 + \dots, \tag{19}$$

where $r_y = L \tan(\theta')$ corresponds to a straight line trajectory. Notice that

Fig. 4. Comparison between the numerically computed (bar), sampled (dashed) and predicted Gaussian (solid) PDFs of the r_y coordinate when $r_x = 1$, with $c_0 = 1$. The three columns indicate the results for three different initial directions $\theta' \in \{0, \pi/8, \pi/4\}$. The two rows show the effect of changing the variance $\sigma_c^2 \in \{0.01, 0.001\}$ on the distribution of r_y values.

$$r_y(\boldsymbol{\epsilon}, 0) = -\frac{L^2}{2c_0}\epsilon_y + \ldots, \tag{20}$$

meaning that the dominant perturbation is independent of both ϵ_x and the second order terms when $\theta' = 0$.

As $|\theta'| \to \pi/2$, the solution for r_y grows without bound (as would be expected) and this growth is faster in the higher order terms. For the leading order terms to dominate the expansion (19), we need to assume that the growth close to $|\theta'| = \pi/2$ is slower than the decay provided by increasing powers of ϵ_x and ϵ_y. For example, a suitable set of requirements for neglecting the second order terms are that $|\epsilon_x| \ll c_0 \cot^2(\theta')/(2L)$ and $|\epsilon_y| \ll c_0|\cot(\theta')|/(2L)$, which become increasingly strong as $|\theta'| \to \pi/2$. Under these assumptions we are able to neglect higher order terms and, as a consequence, conclude that $r_y(\boldsymbol{\epsilon}, \theta')$ samples a normal distribution with mean $\mu_y = L\tan(\theta')$ and variance

$$\sigma_y^2 = \frac{L^4}{4c_0^2}\sec^6(\theta')\sigma_c^2. \tag{21}$$

Here we have used the well-known result for the variance of a linear combination of two independent normally distributed random variables to obtain a closed form expression for σ_y^2. This would not extend more generally to alternative probability distribution models for the material parameter noise (not least because usually one must specify more than simply the mean and variance to obtain the PDF), however, and one would instead need to perform a Monte-Carlo sampling of the formula (19) to estimate the PDF for r_y. Note that a calculation of this type using the normal distribution is shown in the dashed curves of Fig. 4. For alternative choices of probability distribution the PDF for r_y would, in general, only be known numerically, but this would not pose any major issues in terms of its implementation within the boundary integral framework outlined in Section 2. Note that for large values of $|\theta'|$ or σ_c, the above described requirements on $\boldsymbol{\epsilon}$ are less likely to be satisfied, and the higher order terms may have a significant effect on the probability density function. Nevertheless, we have derived an asymptotic model for ray propagation through uncertain media that is valid in the weak noise limit as $\sigma_c \to 0$.

Fig. 4 demonstrates the accuracy of the asymptotic expansion (19) for two choices of the variance $\sigma_c^2 = 0.01$ and $\sigma_c^2 = 0.001$, and three choices of the angle $\theta' = 0, \pi/8$ and $\pi/4$. We fix $c_0 = 1$ and the r_x coordinate of the arrival position to be $r_x = L = 1$. The histograms in Fig. 4 indicate the PDFs given by Monte Carlo simulations of the system (12), which are solved numerically using the fourth order Runge–Kutta method with a sufficiently small time-step to ensure that $|r_x - 1| < 10^{-4}$. The results are shown for a sample of one million ϵ_x and ϵ_y values. The solid line indicates a Gaussian PDF with variance (21). Note that the mean value has been nominally rescaled to zero in all cases. The dashed lines indicate the distribution of the r_y values calculated using the asymptotic expansion (19), truncated after the second order terms explicitly stated in (19), and using a sample of 10 million values of ϵ_x and ϵ_y. Fig. 4 shows that for larger values of θ', these higher order corrections to the Gaussian distribution are necessary to represent the distribution of r_y values unless the variance σ_c^2 is sufficiently small. The sampled PDF in the top right plot of Fig. 4 suddenly cuts off to the left side of the distribution close to $r_y = -0.25$. For the given parameter values, the asymptotic expansion (19) up to the second order minus the mean value
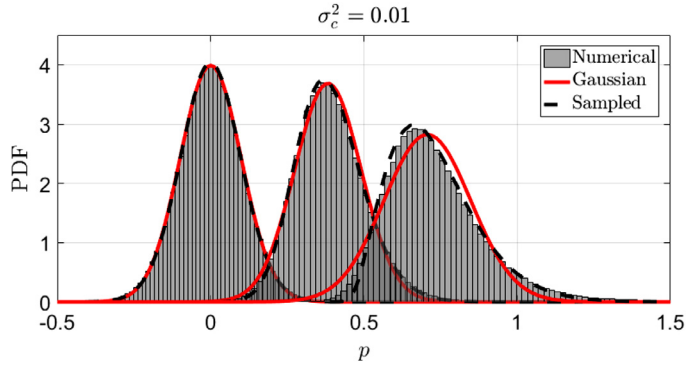
Fig. 5. Comparison between the numerically computed (bar), sampled (dashed) and predicted Gaussian (solid) PDFs for the tangential slowness p, with $c_0 = 1$, $L = 1$ and $\sigma_c^2 = 0.01$. The three distinct results from left to right are for three different initial angles $\theta' \in \{0, \pi/8, \pi/4\}$.

L is

$$r_y(\epsilon, \pi/4) = (\epsilon_x - \epsilon_y) + (\epsilon_x - \epsilon_y)^2.$$

Note that as a function of the variable $\epsilon_x - \epsilon_y$, $r_y(\epsilon, \pi/4)$ has a global minimum of -0.25, which explains the location of the cut off in the top right plot of Fig. 4. Therefore, to improve the accuracy of the sampled distribution in this case requires one to consider even higher order terms in the asymptotic approximation (19).

In addition to the analysis above for the arrival position, Fig. 3 also implies that the specular reflection angles θ at the receiver edges, and hence the tangential slowness $p = c^{-1}\sin(\theta)$ will vary due to the curved trajectories. Using the asymptotic approximation (17) at $t = t^*$ (18) we find

$$p = \frac{1}{c_0}\sin(\theta') - \frac{L}{c_0^2}\sec(\theta')\epsilon_y + \frac{L^2}{2c_0^3}(3\cos^2(\theta') - 1)\sec^3(\theta')\epsilon_x\epsilon_y$$

$$+ \frac{3L^2}{2c_0^3}\tan(\theta')\sec(\theta')\epsilon_y^2 + \ldots \tag{22}$$

up to quadratic order. Note that from simple geometric considerations, the mean reflective angle is equal to θ' and the mean tangential slowness is $c_0^{-1}\sin(\theta')$. Neglecting all higher order terms, then the tangential slowness p at the receiver edge, that is at time t^*, samples a normal distribution with mean $\mu_p^* = c_0^{-1}\sin(\theta')$ and variance

$$\sigma_p^{*2} = \frac{L^2}{c_0^4}\sec^2(\theta')\sigma_c^2. \tag{23}$$

Here, we have again obtained a closed form expression for σ_p^{*2} that does not extend more generally to alternative probability distribution models for the material parameter noise. In this case, one would obtain an asymptotic estimate of the PDF for p numerically by performing a Monte-Carlo sampling of the formula (22). Such a calculation for the normal distribution is shown in the dashed curves of Fig. 5.

We investigate the accuracy of the asymptotic approximation (22) of the tangential slowness for the example above in Fig. 5. We fix the variance $\sigma_c^2 = 0.01$ and consider three choices of θ'. Fig. 5 contains the results of all three experiments with $\theta' = 0$ for the peak to the left, $\theta' = \pi/8$ for the central peak and $\theta' = \pi/4$ for the peak to the right. The histograms indicate the PDFs given by Monte Carlo simulations of the system (12) using the same sample of one million ϵ_x and ϵ_y values as for the histograms in Fig. 4, whereas the solid lines indicate a Gaussian PDF with variance (23). The dashed lines indicate the distributions of the p values calculated using the asymptotic expansion (22), truncated after the second order terms explicitly stated in (22) using the same sample of 10 million ϵ_x and ϵ_y values as in Fig. 4. The results in Fig. 5 follow a similar pattern to the results shown in Fig. 4, that is, for larger values of θ' the higher order corrections to the normal distribution in (22) are necessary to represent the distribution of p to reasonable accuracy (unless the variance σ_c^2 is sufficiently small).

The analysis presented above can also be extended to consider stochastic variations in the trajectory length. To linear order in ϵ_x and ϵ_y, the trajectory length l is given by

$$l = \int_0^{t^*} |\dot{\mathbf{r}}(t)|\, dt = L\sec(\theta') + \frac{L^2}{2c_0}\tan^2(\theta')\sec(\theta')\epsilon_x - \frac{L^2}{2c_0}\tan(\theta')\sec(\theta')\epsilon_y + \ldots.$$

However, for reasons of simplicity, the trajectory length dependent dissipation term $\exp(-\mu d(s, s'))$ described at the end of Section 2 will only be applied with $d(s, s')$ equal to the Euclidean distance between s' and s as before.

3.1.4. Practical implementation algorithm

In the previous section we demonstrated that in the limit of small σ_c, then the arrival positions of the trajectories and the tangential momenta at the receiver edge are normally distributed with variances σ_y^2 (21) and σ_p^{*2} (23), respectively. This model can therefore be implemented approximately within the boundary integral operator formulation of Section 2 by choosing the PDF $f_{\boldsymbol{\sigma}}$ to be an uncorrelated bivariate truncated normal distribution

$$f_{\boldsymbol{\sigma}}\left(X_\varepsilon; X^-, X^+\right) = f_{\sigma_s}\left(s_\varepsilon; s^-, s^+\right) f_{\sigma_p}\left(p_\varepsilon; p^-, p^+\right)$$
$$:= \left(\frac{\chi\left(s_\epsilon; s^-, s^+\right)\exp\left(-\frac{s_\varepsilon^2}{2\sigma_s^2}\right)}{\sqrt{2\pi}\sigma_s\psi_{\sigma_s}(s^-, s^+)}\right)\left(\frac{\chi\left(p_\epsilon; p^-, p^+\right)\exp\left(-\frac{p_\varepsilon^2}{2\sigma_p^2}\right)}{\sqrt{2\pi}\sigma_p\psi_{\sigma_p}(p^-, p^+)}\right) \tag{24}$$

with $\boldsymbol{\sigma} = (\sigma_s, \sigma_p)$ chosen such that $\sigma_s = \sigma_y$ and $\sigma_p = \sigma_p^*$. Here χ restricts $f_{\boldsymbol{\sigma}}$ to (X^-, X^+) via

$$\chi\left(s_\varepsilon; s^-, s^+\right) = H(s^+ - s_\varepsilon) - H(s^- - s_\varepsilon),$$

where H is the Heaviside step function. The functions ψ_{σ_s} and ψ_{σ_p} normalise the PDF so that it satisfies (7) and are given by

$$\psi_{\sigma_s}(s^-, s^+) = \frac{1}{2}\left(\mathrm{erf}\left(\frac{s^+}{\sqrt{2}\sigma_s}\right) - \mathrm{erf}\left(\frac{s^-}{\sqrt{2}\sigma_s}\right)\right), \tag{25}$$

with ψ_{σ_p} defined analogously. A deterministic model with specular reflections is retrieved in the limit $\sigma_s \to 0$ and $\sigma_p \to 0$, whereby $f_{\boldsymbol{\sigma}}$ becomes a two-dimensional Dirac delta distribution. Extending the asymptotic analysis of the previous section to more general PDF models of the material parameter noise would lead to f_{σ_s} and f_{σ_p} being generated numerically at discrete points via Monte-Carlo sampling, and then some form of interpolation between these sample points would be necessary to calculate $f_{\boldsymbol{\sigma}}$ for general noise values X_ε.

Unfortunately, in the form presented in Section 3.1.3, the approach and analysis do not automatically extend to more general propagation speeds (11), or to the convex polygonal domains considered in Section 2. However, if we assume that the arrival position and tangential momentum approximately sample normal distributions, then we can derive an efficient and practical method for computing the parameters σ_s and σ_p with any given propagation speed (11), which we detail below. As before, the extension to alternative probability distributions will also be possible leading to numerically sampled, rather than closed form PDFs in general.

We will apply our method on closed convex polygonal domains where the receiver edges are of finite length. The spatial support of $f_{\boldsymbol{\sigma}}$, denoted earlier as (s^-, s^+), will be limited to the target edge of the deterministic map φ as depicted in Fig. 1, in order to improve the tractability of the approach. We note that this is also the same boundary integral model considered in Ref. [27]. Let the receiver edge on a convex polygon Ω have endpoints with position vectors $\mathbf{a} = (a_x, a_y)$ and $\mathbf{b} = (b_x, b_y)$. Then the edge obeys the straight-line equation

$$(b_x - a_x)y = (b_y - a_y)x + (b_x a_y - a_x b_y),$$

which we write more concisely in the form $\alpha y = \beta x + \gamma$. We need to find the parameters σ_s and σ_p for each receiver coordinate $X = (s, p)$ on this edge. We trace back along the deterministic flow map φ to find the starting position s' and corresponding tangential slowness p', that is, $X' = (s', p')$. From X' we can find the initial trajectory position $\mathbf{r}_0 = (r_{x0}, r_{y0})^T$ and the unit momentum vector $\mathbf{p}_0 = (p_{x0}, p_{y0})^T$. Given $\mathbf{r}_0$ and $\mathbf{p}_0$, the ray trajectory can be approximated by the asymptotic expansion (13) for any propagation speed (11). To proceed further we need to find the arrival time t^* of these trajectories at the edge given by $\alpha y = \beta x + \gamma$ and compute the integrals (15). To make this tractable, we consider the asymptotic expansion for the arrival time (18) up to first order, i.e.

$$t^* = t_0 + t_x\epsilon_x + t_y\epsilon_y + \ldots, \tag{26}$$

where t_x, t_y are unknown expansion coefficients and

$$t_0 = \frac{\beta r_{x0} - \alpha r_{y0} - \gamma}{c_0(\beta p_{x0} - \alpha p_{y0})}$$

is the arrival time corresponding to the deterministic straight-line trajectory. It can be shown that to the zeroth order (sufficient when considering the (truncated) Gaussian PDF), the matrix perturbation functions (13) at the arrival time $t = t^*$ are

$$\bar{\boldsymbol{R}}(t^*) = \bar{\boldsymbol{R}}(t_0) + \ldots = \int_0^{t_0}\left(2\boldsymbol{p}_0 \otimes \bar{\mathbf{c}}(\boldsymbol{r}_0 + c_0\boldsymbol{p}_0\tau) + c_0^2\bar{\boldsymbol{P}}(\tau)\right)d\tau + \ldots,$$

$$\bar{\boldsymbol{P}}(t^*) = \bar{\boldsymbol{P}}(t_0) + \ldots = -\frac{1}{c_0}\int_0^{t_0}\nabla\bar{\mathbf{c}}(\boldsymbol{r}_0 + c_0\boldsymbol{p}_0\tau)d\tau + \ldots \tag{27}$$

To find the perturbation coefficients t_x and t_y, we impose that the asymptotic trajectory (13) crosses the receiver edge where $\alpha y = \beta x + \gamma$ at the arrival time t^* (26) and thus

$$\begin{pmatrix} t_x \\ t_y \end{pmatrix} = \frac{c_0^{-1}}{\alpha p_{y0} - \beta p_{x0}}\bar{\boldsymbol{R}}(t_0)^T\begin{pmatrix} \beta \\ -\alpha \end{pmatrix}. \tag{28}$$

Then at time $t = t^*$ we find that

$$
\begin{aligned}
\boldsymbol{r}(t^*) &= \boldsymbol{r}_0 + c_0 \boldsymbol{p}_0 t^* + \bar{\boldsymbol{R}}(t^*)\boldsymbol{\epsilon} + \ldots \\
&= \boldsymbol{r}_0 + c_0 \boldsymbol{p}_0 t_0 + c_0 \boldsymbol{p}_0 (t_x, t_y)\boldsymbol{\epsilon} + \bar{\boldsymbol{R}}(t_0)\boldsymbol{\epsilon} + \ldots .
\end{aligned}
$$

Using the expression (28) for (t_x, t_y) and introducing the mean arrival position $\boldsymbol{r}_d = \boldsymbol{r}_0 + c_0 \boldsymbol{p}_0 t_0$ then leads to

$$
\begin{aligned}
\boldsymbol{r}(t^*) &= \boldsymbol{r}_d + \frac{1}{\alpha p_{y0} - \beta p_{x0}} \boldsymbol{p}_0 (\beta, -\alpha) \bar{\boldsymbol{R}}(t_0)\boldsymbol{\epsilon} + \bar{\boldsymbol{R}}(t_0)\boldsymbol{\epsilon} + \ldots \\
&= \boldsymbol{r}_d + \frac{1}{\alpha p_{y0} - \beta p_{x0}} \begin{pmatrix} \alpha p_{y0} & -\alpha p_{x0} \\ \beta p_{y0} & -\beta p_{x0} \end{pmatrix} \bar{\boldsymbol{R}}(t_0)\boldsymbol{\epsilon} + \ldots \\
&= \boldsymbol{r}_d + \boldsymbol{A}\bar{\boldsymbol{R}}(t_0)\boldsymbol{\epsilon} + \ldots .
\end{aligned}
\tag{29}
$$

To find σ_s from (29), we find a rotation matrix Θ such that after rotation all positions $\boldsymbol{r}(t^*)$ are on the line parallel to the y-axis, that is

$$
\Theta \boldsymbol{r}(t^*) = \Theta \boldsymbol{r}_d + \Theta \boldsymbol{A} \bar{\boldsymbol{R}}(t_0)\boldsymbol{\epsilon} + \ldots .
\tag{30}
$$

Denoting $\boldsymbol{B} = \Theta \boldsymbol{A} \bar{\boldsymbol{R}}(t_0)$, then from the y-component we find that

$$
\sigma_s^2 = (\boldsymbol{B}_{2,1}^2 + \boldsymbol{B}_{2,2}^2)\sigma_c^2.
\tag{31}
$$

Notice that σ_s^2 depends on the sum of the squares of the entries of $\boldsymbol{B}$. We may estimate this sum using the Frobenius norm:

$$
\|\boldsymbol{B}\|_F^2 = \|\Theta \boldsymbol{A} \bar{\boldsymbol{R}}(t_0)\|_F^2 \leq \|\Theta\|_F^2 \|\boldsymbol{A}\|_F^2 \|\bar{\boldsymbol{R}}(t_0)\|_F^2 \leq 2\|\boldsymbol{A}\|_F^2 \|\bar{\boldsymbol{R}}(t_0)\|_F^2,
$$

where

$$
\|\boldsymbol{A}\|_F^2 = \frac{\alpha^2 + \beta^2}{(\alpha \sin(\theta') - \beta \cos(\theta'))^2},
$$

and $\boldsymbol{p}_0 = (\cos(\theta'), \sin(\theta'))^T$ as before. The Frobenius norm of the matrix $\boldsymbol{A}$ therefore becomes unbounded at values of θ' where the mean reflective angle at the receiver edge approaches $\pm \pi/2$. The Frobenius norm of the matrix $\bar{\boldsymbol{R}}(t_0)$ will depend on the parameter values for a given example, including the propagation speed (11). In the case of alternative PDF models for the material parameter noise we would obtain a numerical estimate of the PDF for the arrival position via a Monte-Carlo sampling of the formula (30).

To find the parameter σ_p for the tangential slowness, we use the formula (27) to obtain

$$
\boldsymbol{p}(t^*) = \frac{1}{c_0} \boldsymbol{p}_0 + \bar{\boldsymbol{P}}(t^*)\boldsymbol{\epsilon} + \ldots = \frac{1}{c_0} \boldsymbol{p}_0 + \bar{\boldsymbol{P}}(t_0)\boldsymbol{\epsilon} + \ldots .
$$

Considering the tangential component of $\boldsymbol{p}$, we find that

$$
p = \frac{\boldsymbol{p}_0 \cdot \boldsymbol{\nu}}{c_0} + (\bar{\boldsymbol{P}}(t_0)\boldsymbol{\epsilon}) \cdot \boldsymbol{\nu} + \ldots ,
\tag{32}
$$

and thus we obtain

$$
\sigma_p^2 = \left| \bar{\boldsymbol{P}}(t_0)^T \boldsymbol{\nu} \right|^2 \sigma_c^2,
\tag{33}
$$

where $\boldsymbol{\nu}$ is the normalized direction vector of the receiver edge. As before, to extend to alternative PDF models for the material parameter noise we would apply a Monte-Carlo sampling of the formula (32) leading to a numerical estimate of the PDF for p.

The method to find the parameters σ_s (31) and σ_p (33) described above may be applied to any convex polygonal domain with propagation speed (11). We will adopt this approach for performing numerical examples with an uncertain propagation speed c in Section 4.1.

3.2. Uncertain geometry

In this section we consider geometric uncertainties in two respects. Firstly, we model the case when the position of an entire region of the boundary Γ is uncertain. For example, if the measured length of a rectangular plate was subject to error, which can be modelled probabilistically. Secondly, we consider small scale uncertain fluctuations of the geometry leading to rough edge reflections.

3.2.1. Positional uncertainties

The position of a boundary edge of Γ receiving a propagated trajectory may be considered as uncertain. We consider the relatively simple case where the edge is parallel to the mean edge position and follows a normal distribution $\epsilon_\perp \sim \mathcal{N}(0, \sigma_\perp^2)$, $\epsilon_\parallel \sim \mathcal{N}(0, \sigma_\parallel^2)$, where $\epsilon_\perp$ and $\epsilon_\parallel$ denote the displacement from the mean edge position in the directions perpendicular and tangential to the edge, respectively. These modelling assumptions are for the purposes of permitting some initial analytic progress in the derivation of the uncertainty model, but are not restrictions on the applicability of the approach in general. Extensions to less restrictive assumptions on the geometry and alternative PDFs for the perturbation about the mean are topics for further work in this area. We note that, as before, normal distributions are an appropriate choice here under the assumptions of symmetry about the mean and that the edge position is more likely to be close to the mean than far away.

Assuming that the length of the edge is fixed, then it is relatively straightforward to derive (from geometrical considerations) that the boundary position arclength parametrisation s is given by

$$s = \bar{s} + \epsilon_\perp \tan(\theta) - \epsilon_\parallel. \tag{34}$$

Here $\bar{s}$ denotes the boundary position arclength parametrisation of the mean boundary edge and as before, θ denotes the angle of the ray after specular reflection at the uncertain boundary, measured with respect to the surface normal vector at the arrival position. Hence the deviation of the boundary edge coordinate about the mean $\bar{s}$ is normally distributed with variance $\sigma_\perp^2 \tan^2(\theta) + \sigma_\parallel^2$, again using standard properties of linear combinations of normally distributed random variables. This model can therefore be approximated within the stochastic transfer operator framework introduced in Section 2 with the truncated normal distribution PDF (24) and setting $\sigma_s^2 = \sigma_\perp^2 \tan^2(\theta) + \sigma_\parallel^2$. This leads to an approximation that is valid as $\sigma_\perp$, $\sigma_\parallel \to 0$, since then the truncated normal distributions more closely approximate normal distributions. As in the previous section, a straightforward method for extending the above analysis beyond normally distributed noise would be to apply Monte-Carlo sampling in the formula (34) and approximate the PDF for the boundary edge coordinate numerically.

3.2.2. Directional uncertainties

The PDF (24), or any appropriate alternative, may be applied to model stochastic rough boundary reflections according to the choice of parameter σ_p. For convex polygonal domains, we may compute the spatial integral in (5) analytically (see Section 4.1) and the result is bounded for $\sigma_s = 0$. This type of geometric uncertainty can therefore be modelled by taking $\sigma_s = 0$ and considering the influence of the parameter σ_p alone. The limiting cases of small and large σ_p are well understood and the transition from infinitesimally small to infinitely large σ_p corresponds to the transition from specular to Lambertian reflections at the boundary. We note that the property of interpolating between specular and Lambertian reflections is common within rough surface reflection models for geometrical optics, such as the well-known Phong reflection model [29]. In the case of infinitesimally small σ_p the correspondence is reasonably clear since in the limit $\sigma_p \to 0$, the term $f_{\sigma_p}(p_\varepsilon; p^-, p^+)$ from the PDF (24) tends to $\delta(p - \varphi_p(X'))$, where the tangential slowness component of the deterministic boundary map φ_p corresponds to a specular reflection as before. In the limit $\sigma_p \to \infty$, then $f_{\sigma_p}(p_\varepsilon; p^-, p^+) \to c/2$ and thus one obtains a uniform distribution in p. We note that this corresponds to a Lambertian (cosine) distribution in the reflection angle since a change of variables from p to θ gives

$$\int_{-c^{-1}}^{c^{-1}} \frac{c}{2}\, dp = \int_{-\pi/2}^{\pi/2} \frac{\cos(\theta)}{2}\, d\theta = 1. \tag{35}$$

We will investigate this reflection behaviour numerically in the Section 4.2.

3.3. Uncertain sources

In this section we discuss the source boundary densities ρ_0 used to drive the system (9). In the case of a high-frequency wave problem, the source boundary density may be derived from the source or boundary conditions prescribed in the underlying wave problem. We first consider an excitation from a point source with an uncertain location. The acoustic energy density ρ_0 on the boundary Γ arising from a velocity potential point source of angular frequency ω located at $\mathbf{r}_0^* = (x_0^*, y_0^*) \in \Omega$ and is given by [30]

$$\rho_0(s, p; \mathbf{r}_0^*) = \frac{\omega \rho^f \cos(\vartheta(\mathbf{r}_s, \mathbf{r}_0^*)) \exp(-\mu|\mathbf{r}_s - \mathbf{r}_0^*|)\delta(p - p_0^*)}{8\pi |\mathbf{r}_s - \mathbf{r}_0^*|}. \tag{36}$$

Here ρ^f is the density of the fluid medium, μ is the damping coefficient as before and $\vartheta(\mathbf{r}_s, \mathbf{r}_0^*)$ is the negative of the angle between the direction vector $\mathbf{r}_0^* - \mathbf{r}_s$ and the interior normal vector at s. In addition, $p_0^* = \sin(\vartheta(\mathbf{r}_s, \mathbf{r}_0^*))/c$ is the tangential slowness of the trajectory arriving at $s \in \Gamma$ from the source point $\mathbf{r}_0^* \in \Omega$ and $\mathbf{r}_s$ gives the Cartesian coordinates of the point $s \in \Gamma$ as before.

In order to generalise the deterministic point source described above to a stochastic one, we consider a disc D_R with centre $\mathbf{r}_0^*$ and radius R chosen such that $D_R \subset \Omega$. We then replace the source point with a truncated normal distribution inside D_R, where the probability decreases as the radial distance from $\mathbf{r}_0^*$ increases from $r = 0$ towards $r = R$. Explicitly, we obtain

$$\rho_0(s, p; D_R) = \int_0^{2\pi} \int_0^R \frac{\omega \rho^f \cos(\vartheta(\mathbf{r}_s, \mathbf{r}_0)) \exp(-\mu|\mathbf{r}_s - \mathbf{r}_0| - r^2/(2\sigma_0^2))\delta(p - p_0)}{16\pi^2 \sigma_0^2 (1 - \exp(-R^2/(2\sigma_0^2)))|\mathbf{r}_s - \mathbf{r}_0|} r\, dr\, d\phi, \tag{37}$$
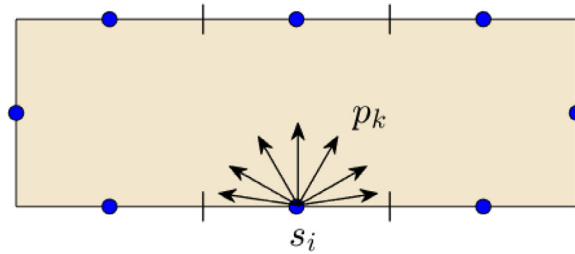
Fig. 6. A domain Ω with boundary Γ divided into elements. The collocation points for the spatial variable s are represented by dots at the element midpoints. The collocation points for the tangential slowness p are represented by the arrows.

where (r, ϕ) are polar coordinates in D_R that govern the location of the source point $\mathbf{r}_0 = (x_0, y_0) = (x_0^* + r\cos\phi, y_0^* + r\sin\phi)$. Also, σ_0 is the standard deviation of the underlying normal distribution before truncation/scaling and $p_0 = \sin(\vartheta(\mathbf{r}_s, \mathbf{r}_0))/c$. In addition, we may incorporate uncertain (or rough) boundary reflections in Eq. (37) By replacing the delta distribution $\delta(p - p_0)$ with a truncated Gaussian distribution of the form

$$\frac{\exp\left(-(p - p_0)^2/(2\sigma_p^2)\right)}{\sqrt{2\pi}\sigma_p \psi_{\sigma_p}(-c^{-1} - p_0, c^{-1} - p_0)}, \tag{38}$$

which tends to $\delta(p - p_0)$ in the limit as $\sigma_p \to 0$. Similarly, the effect of uncertain boundary arrival positions from a given source point may be included via an additional integral over the boundary Γ and multiplying the integrand by the PDF of a truncated normal distribution in the spatial variable s.

Alternatively we may consider source terms arising from uncertain boundary conditions. An example of such source term was proposed in Ref. [4] and takes the form

$$\rho_0(s, p) = \frac{\exp\left(-p^2/(2\sigma_b^2)\right)\chi(s; \Gamma_0)}{\sqrt{2\pi\sigma_b^2}\,\mathrm{erf}\left(1/(\sqrt{2}\sigma_b c)\right)}, \tag{39}$$

where χ is a cut-off function restricting the support of ρ_0 to a subset of the boundary $\Gamma_0 \subseteq \Gamma$. Again our model is based on a truncated normal distribution, where the underlying normal distribution before truncation/scaling has mean 0 and standard deviation σ_b. For small σ_b, (39) describes a unit boundary density dominated by its mean tangential slowness $p = 0$, that is, propagating parallel to the normal vector. If we instead consider large σ_b, then (39) describes Lambertian propagation (uniformly distributed in p). This type of source term was applied on a subset Γ_0 of Γ in Ref. [4] and a homogeneous boundary condition was imposed over the remaining part of Γ. Note that in this section we have again based our models on the truncated normal distribution due to its convenient property of interpolating between a deterministic model and a uniform distribution in different parameter limits, but alternatives would be relatively straightforward to implement here.

4. Implementation and numerical results

In this section we describe the discretisation of the phase-space boundary integral model introduced in Section 2. We then consider three numerical examples illustrating the model uncertainties introduced in Section 3.

4.1. Discretisation

In this section we summarise the collocation discretisation of Eq. (9) originally proposed in Ref. [27]. For illustration purposes we consider a single polygonal domain, such as the one depicted in Fig. 6. The spatial variable s is discretised using a piecewise constant boundary element basis approximation, which has the advantage that the spatial integral appearing in $\mathcal{L}_\sigma$ (5) is simplified to the extent where it can be evaluated analytically. A collocation method using a (globally supported) basis of scaled Legendre polynomials $\phi_l(p)$, $l = 1, \ldots, N + 1$, is employed to discretise with respect to the tangential slowness p. We note that this combination is a good choice for problems where the solution has a low degree of regularity in a relatively complex spatial domain compared to a smoother dependence on p in the simple interval domain $(-c^{-1}, c^{-1})$. In the latter case, orthogonal polynomials are a popular choice for due to their spectral convergence for smooth functions [31]. The energy density $\rho_\infty(X)$ may therefore be approximated on the boundary phase-space Q in the form

$$\rho_\infty(X) \approx \sum_{j=1}^{n} \sum_{l=1}^{N+1} \rho_{j,l} b_j(s) \phi_l(p), \tag{40}$$

where

$$b_j(s) = \begin{cases} 1 & \text{if } s \in I_j, \\ 0 & \text{otherwise}, \end{cases}$$

and I_j, $j = 1, 2, \ldots, n$ denotes the sub-intervals for the arclength coordinate $s \in \Gamma$ corresponding to a set of n boundary elements. The goal is to determine the coefficients $\rho_{j,l}$ for $j = 1, 2, \ldots, n$ and $l = 1, 2, \ldots, N + 1$.

Substituting the approximation (40) into (5) for ρ_∞, we obtain

$$
\begin{aligned}
\mathcal{L}_\sigma \rho_\infty(X) &\approx \sum_{j=1}^{n} \sum_{l=1}^{N+1} \rho_{j,l} \int_Q f_\sigma(X - \varphi(X')) b_j(s') \phi_l(p') \, dX' \\
&= \sum_{j=1}^{n} \sum_{l=1}^{N+1} \rho_{j,l} \int_{-c^{-1}}^{c^{-1}} \phi_l(p') \left[\int_{I_j} f_\sigma(X - \varphi(X')) \, ds' \right] dp'.
\end{aligned}
$$

Applying the PDF f_σ chosen in (24) the yields

$$
\begin{aligned}
\mathcal{L}_\sigma \rho_\infty(X) &\approx \sum_{j=1}^{n} \sum_{l=1}^{N+1} \rho_{j,l} \int_{-c^{-1}}^{c^{-1}} \phi_l(p') f_{\sigma_p}(p_\varepsilon) \left[\int_{I_j} f_{\sigma_s}(s_\varepsilon) \, ds' \right] dp' \\
&= \sum_{j=1}^{n} \sum_{l=1}^{N+1} \rho_{j,l} \int_{-c^{-1}}^{c^{-1}} \phi_l(p') f_{\sigma_p}(p_\varepsilon) \left[\frac{-1}{2\psi_{\sigma_s}(s^-, s^+)} \mathrm{erf}\left(\frac{s - \varphi_s(X')}{\sqrt{2}\sigma_s} \right) \Bigg|_{s'_{\min}(p')}^{s'_{\max}(p')} \right] dp',
\end{aligned} \tag{41}
$$

where, in the second line, we have evaluated the spatial integral explicitly as a function of p', and $\varphi_s(X')$ is the spatial component of $\varphi(X')$ defined in Eq. (6). Note that the notation $s'_{\min}$ and $s'_{\max}$ has been introduced since the limits will not, in general, correspond to the endpoints of I_j when the pre-image φ^{-1} of a vertex of Γ intersects I_j (for a given p'). An analytic (but non-elegant) solution also exists for the spatial integral in the case of an additional damping factor $\exp(-\mu d(s, s'))$, with notation as in Section 2, where the result is a product of the error and exponential functions.

Let the spatial collocation points be denoted s_i, $i = 1, \ldots, n$, and choose them to be the mid-points of the corresponding boundary elements as depicted in Fig. 6. In the direction variable, we choose the Chebyshev points

$$
p_k = c^{-1} \cos\left(\frac{2k - 1}{2(N + 1)} \pi \right), \qquad k = 1, \ldots, N + 1,
$$

for the collocation points, leading to an equi-spaced set of collocation directions

$$
\theta_k = \frac{\pi}{2} - \frac{2k - 1}{2(N + 1)} \pi.
$$

The full discretization of the stochastic transfer operator (5) is therefore given by $(\mathcal{L}_\sigma \rho_\infty)(s_i, p_k) \approx \boldsymbol{L}\boldsymbol{\rho}$, where the vector

$$
\boldsymbol{\rho} = [\rho_{1,1} \ \rho_{1,2} \cdots \rho_{1,N+1} \ \rho_{2,1} \cdots \rho_{n,N+1}]^T
$$

and the matrix $\boldsymbol{L}$ has entries

$$
\boldsymbol{L}_{(i,k),(j,l)} = c^{-1} \int_{-\pi/2}^{\pi/2} \phi_l(p'(\theta')) f_{\sigma_p}(p_\varepsilon(p_k, X')) S_\mu^j(s_i, X') \cos(\theta') \, d\theta', \tag{42}
$$

with $p_\varepsilon(p_k, X') = p_k - \varphi_p(X')$ for $i, j = 1, \ldots, n$ and $k, l = 1, \ldots, N + 1$. Here, we have applied the change of variables $\theta' = \sin^{-1}(cp')$ and introduced the notation S_μ^j for the analytic solution of the spatial integral with damping factor μ over the jth boundary element. Note that whilst the PDF f_σ becomes unbounded as $\sigma_s \to 0$, the spatial integral S_μ^j is well defined in this limit. The integral appearing in Eq. (42) will be computed numerically using adaptive Clenshaw-Curtis quadrature as detailed in Ref. [27]. The main advantage of this choice is that one obtains a spectrally convergent quadrature rule provided that the integral has been subdivided into a sum of several integrals, each with a smooth integrand. This is a consequence of the fact that the function S_μ^j is smooth except at a finite number of discrete points, see Ref. [27] for further details.

Once the stochastic transfer operator (5) has been discretised as detailed above, the integral Eq. (9) may then be written in discrete form as the linear system

$$
(\boldsymbol{K} - \boldsymbol{L})\boldsymbol{\rho} = \boldsymbol{K}\boldsymbol{\rho}_0. \tag{43}
$$

Here $\boldsymbol{K}$ is the interpolation matrix for the collocation projection whereby

$$
\boldsymbol{K}\boldsymbol{\rho} = [\rho_\infty(s_1, p_1) \ \rho_\infty(s_1, p_2) \cdots \rho_\infty(s_1, p_{N+1}) \ \rho_\infty(s_2, p_1) \cdots \rho_\infty(s_n, p_{N+1})]^T.
$$

Due to the local nature of the spatial basis functions, K will be a block sparse matrix made up of n non-zero blocks along the diagonal with entries $\{\phi_l(p_k)\}_{k,l=1,\ldots,N+1}$. In the next section we employ the above described collocation based discretisation strategies to perform numerical experiments which illustrate the model uncertainties introduced in Section 3.

4.2. Numerical results

In this section we study three numerical examples to illustrate the uncertainty models presented in Section 3. We note that the verification of both the boundary integral model introduced in Section 2 and its discretisation via the collocation

approach detailed in Section 4.1 have been presented in Ref. [27], including a comparison with exact and reference numerical solutions and a systematic convergence study. One typically observes linear convergence as the boundary element mesh size h is decreased and spectral convergence as the order of the Legendre polynomial basis in the momentum variable is increased. The verification and convergence properties are not the focus of the present study and hence they are not considered further here. In what follows, we therefore only perform simulations with the discretisation parameters fixed where the solutions have converged sufficiently so that doubling the number of collocation points in both variables provides a visually identical solution. We fix the number of collocation points to be $N = 128$ in the direction variable p and the damping coefficient $\mu = 1$. We introduce a new parameter Δ, which indicates the length of the shortest edge of the polygon Ω. In the following examples we take the average length of the boundary elements to be $h = \Delta/6$.

In the first example we will consider a convex polygon $A'B'C'D'$ with vertices $A' = (0,0)$, $B' = (0.75, -0.25)$, $C' = (0.75, 0.5)$ and $D' = (0, 0.25)$ and thus $\Delta = 0.25$. In the remaining two examples we will consider the polygon $ABCDEF$ illustrated in Fig. 1 with vertices $A = (0,0)$, $B = (0.65, 0)$, $C = (0.75, 0.1)$, $D = (0.7, 0.35)$, $E = (0.2, 0.35)$ and $F = (0, 0.2)$ with $\Delta = 0.1\sqrt{2}$. Taking $h = \Delta/6$ then leads to a total of $n = 62$ boundary elements on the first polygon $A'B'C'D'$ and $n = 75$ boundary elements on the polygon $ABCDEF$. In addition, the arc-length parameter s for both polygonal boundaries runs anticlockwise starting at the vertex $A' = A = (0,0)$.

We first consider the modelling of uncertain material parameters as described in Section 3.1. In particular, we consider an uncertain propagation speed of the form (11) inside the polygon $A'B'C'D'$, given by $c(\boldsymbol{r}) = 1 + \boldsymbol{\epsilon} \cdot \boldsymbol{r}$, that is we take $c_0 = 1$ and $\bar{\boldsymbol{c}}(\boldsymbol{r}) = \boldsymbol{r}$. The parameters σ_s and σ_p are computed for each pair of spatial and directional collocation points as a preprocessing step using the formulæ (31) and (33), respectively. Recall that the σ_s and σ_p values depend on σ_c, and tend to zero when $\sigma_c \to 0$. In Fig. 7 we show the results of four computations, each with a different σ_c value in the range from 0.01 to 1. For $\sigma_c = 0.01$, we illustrate a close to deterministic solution and for larger σ_c values we demonstrate the effects of increased uncertainty in the propagation speed c. Note that with large values of σ_c the asymptotic analysis of Section 3.1 becomes invalid and $f_{\boldsymbol{\sigma}}$ (24) describes propagation to all admissible positions (i.e. a particular target edge, see Fig. 1) and tangential momenta with equal probability as shown in Fig. 8.

To obtain the results shown in Figs. 7 and 8, we prescribe an uncertain boundary source (39) along the edge $\Gamma_0 = D'A'$ with $c = c_0 = 1$ and $\sigma_b = 0.01$. In the left column of Fig. 7 we illustrate the polygon $A'B'C'D'$ and along the boundaries we plot $\tilde{\rho}_\infty$, which is the integral over the tangential slowness p of the boundary density ρ_∞, that is,

$$\tilde{\rho}_\infty(s) = \int_{-1}^{1} \rho_\infty(s, p)\, \mathrm{d}p = \sum_{j=1}^{n} \sum_{l=1}^{N+1} \rho_{j,l} b_j(s) \int_{-1}^{1} \phi_l(p)\, \mathrm{d}p = 2 \sum_{j=1}^{n} \rho_{j,1} b_j(s).$$

In the right column of Fig. 7 we plot the stationary boundary density minus the initial boundary density, that is, $\rho_\infty(s, p) - \rho_0(s, p)$. The contribution of the initial density has been removed to better illustrate the fine details of the indirect, or reverberant, part of the solution (the part not emanating directly from the source term) that would otherwise be suppressed in the plot due to the damping.

The case $\sigma_b = \sigma_c = 0.01$ is shown in the top row of Fig. 7 and illustrates an approximately deterministic solution. Here, the behaviour is dominated by rays that travel parallel to the x-axis from the initial density ρ_0 on the left edge $D'A'$, and reflect specularly upon reaching the edge $B'C'$ to then travel back parallel to the x-axis and so on. The remaining rows of Fig. 7 show the effects of increasing uncertainty in the propagation speed c. As σ_c is increased, the uncertainty in the arrival position on the edge $B'C'$ increases as demonstrated by spreading of the energy across the edge $B'C'$ in the left column of Fig. 7. Since the rays will not necessarily travel in straight lines, then the uncertainty in the tangential slowness p also consequently increases as shown in the right column of Fig. 7, where the boundary density spreads across all values of p. If we continue increasing σ_c further, then we observe propagation to all positions on a particular receiver edge and all tangential momenta with equal probability. Fig. 8 illustrates this point and shows the results of simulations for $\sigma_c = 10$ and $\sigma_c = 100$. We recall that the influence of the initial density ρ_0 has been removed from the plot and hence the largest values of

$$\rho_\infty - \rho_0 = \sum_{j=1}^{\infty} (\mathcal{L}_{\boldsymbol{\sigma}})^{(j)} \rho_0 \tag{44}$$

are observed on the target edge of $\mathcal{L}_{\boldsymbol{\sigma}} \rho_0$ (that is, edge $B'C'$) and arise from the $j = 1$ term in the sum (44). This is due to the fact that the damping term $\exp(-d(s, s'))$, where d is the Euclidean distance from s' to s as before, has a stronger effect as j is increased because the damping losses accumulate through successive iterates of $\mathcal{L}_{\boldsymbol{\sigma}}$ in the later contributions ($j > 1$) to the sum (44).

We now consider the modelling of geometric uncertainties as described in Section 3.2.1. We perform numerical simulations for the polygon $ABCDEF$ shown in Fig. 1 with constant propagation speed $c = 1$ and fix $\sigma_p = 0.01$. A deterministic source point (36) placed at $(0.15, 0.1)$ is used to excite the system for different values of $\sigma_\perp$ and $\sigma_\parallel$. Recall that the parameters $\sigma_\perp$ and $\sigma_\parallel$ control the level of uncertainty in the boundary geometry and for convenience we will restrict to the case $\sigma_\perp = \sigma_\parallel$.

The left column of Fig. 9 shows the natural logarithm of the stationary interior density ρ_Ω (10) inside the polygon $ABCDEF$ for $\sigma_\perp = \sigma_\parallel = 0.01$ (top row), 0.1 (middle row) and 1 (bottom row). The right column shows the corresponding result after removing the direct contribution from the (point) source density ρ_0 in order to more clearly show the behaviour
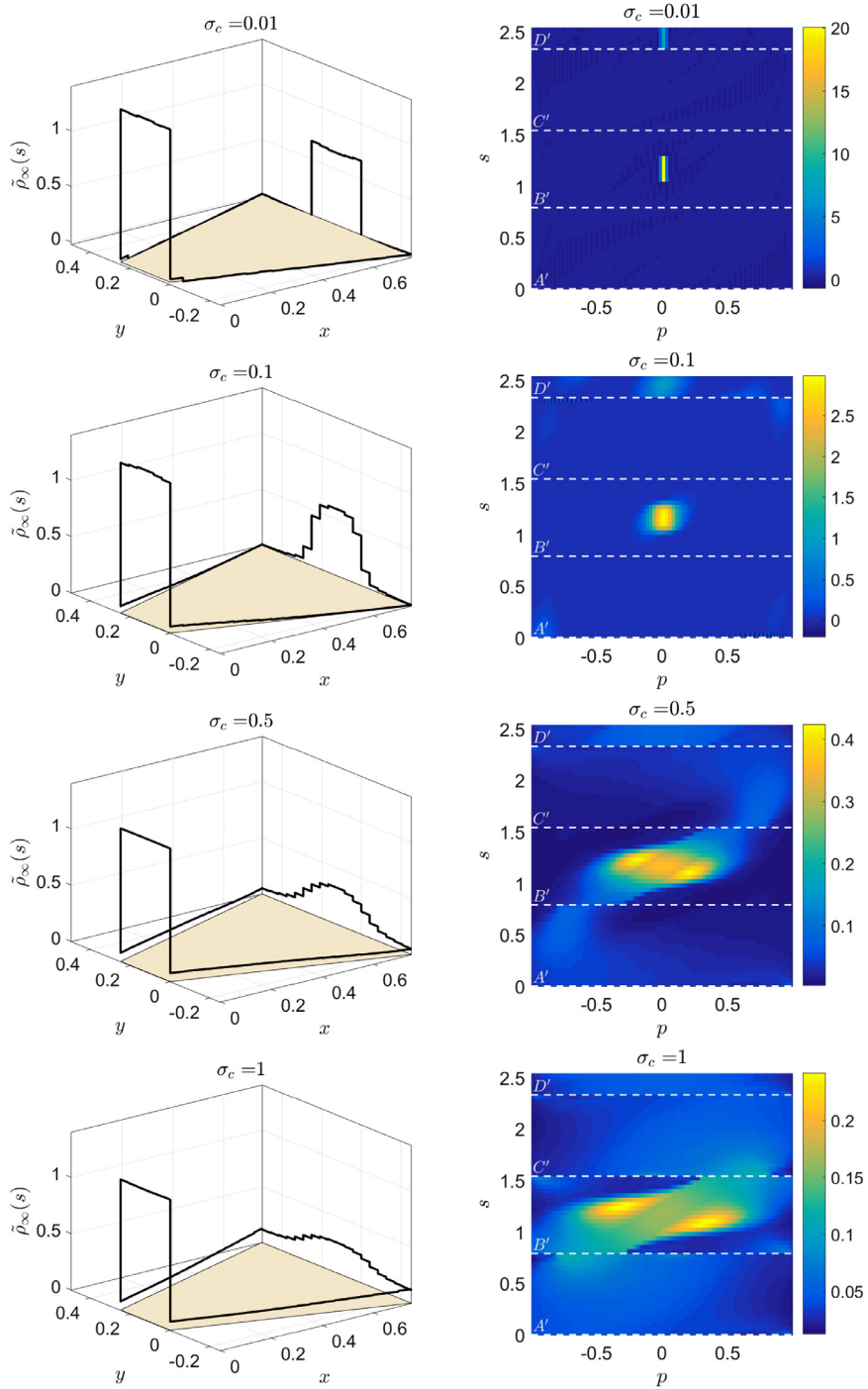
Fig. 7. Uncertain propagation speed simulations with four different values of the propagation speed variance σ_c^2. Left: the stationary boundary density ρ_∞ integrated with respect to the tangential slowness p. Right: stationary boundary density minus the initial density $(\rho_\infty - \rho_0)(s, p)$, where the white dashed lines indicate the vertices of the polygon $A'B'C'D'$. Parameter values: $c_0 = 1$, $\bar{c}(r) = r$, $\sigma_b = 0.01$, $\mu = 1$, $h = 1/24$ and $N = 128$.

of the indirect/reverberant field. The simulation with $\sigma_\perp = \sigma_\parallel = 0.01$ is an approximate representation of the deterministic solution, which is evident from the strongly directive ray paths with specular reflections. As the $\sigma_\perp$ and $\sigma_\parallel$ values increase, the interior density distribution becomes smoother while retaining a similar background structure, but with the more rapidly varying fluctuations removed.
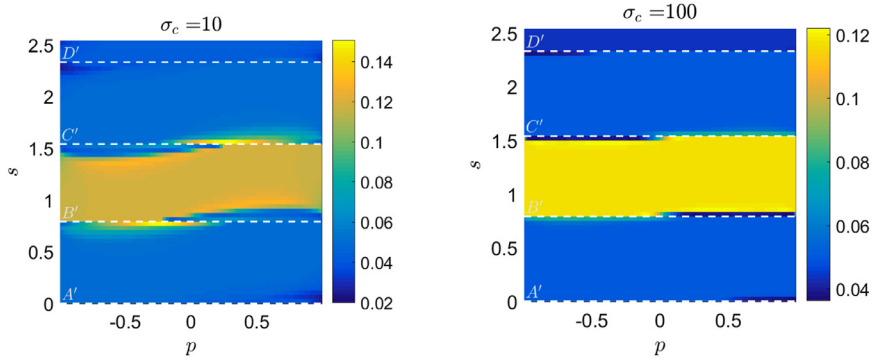
Fig. 8. Uncertain propagation speed simulations with $\sigma_c = 10$ and $\sigma_c = 100$. Stationary boundary density minus the initial density $(\rho_\infty - \rho_0)(s, p)$, where the white dashed lines indicate the vertices of the polygon $A'B'C'D'$. Parameter values: $c_0 = 1$, $\bar{c}(\boldsymbol{r}) = \boldsymbol{r}$, $\sigma_b = 0.01$, $\mu = 1$, $h = 1/24$ and $N = 128$.
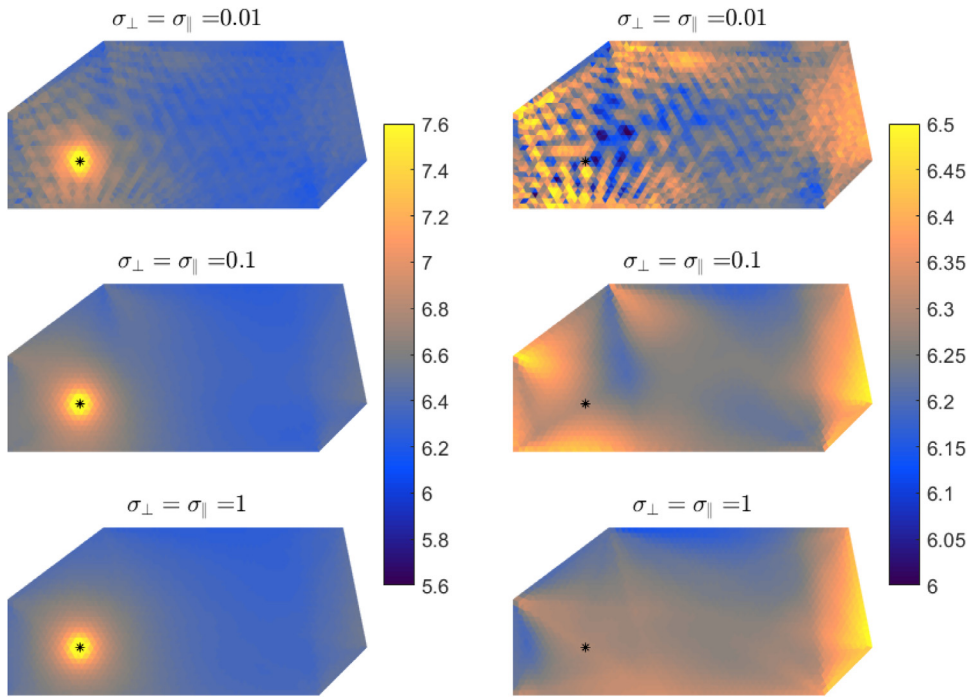

Fig. 9. Uncertain geometry simulation for different values of $\sigma_\perp = \sigma_\parallel$. The plots show the logarithm of the stationary interior density including the direct source contribution (left) and the reverberant field without the direct source contribution (right). The point source located at (0.15,0.1) is indicated by a black dot. Parameter values: $c = 1$, $\sigma_0 = 0$, $\sigma_p = 0.01$, $\mu = 1$, $h = \sqrt{2}/60$ and $N = 128$.

In the final numerical example we combine the modelling of rough surface reflections, as discussed in Section 3.2.2, together with the modelling of uncertain point sources (37) as described in Section 3.3. We consider the polygon *ABCDEF* as above, with a mean point source location $\boldsymbol{r}_0^* = (0.15, 0.1)$, see Section 3.3. We set $\sigma_s = 0$, meaning that the ray propagation with respect to the position variable s is treated deterministically. We consider a range of values for the parameter σ_p in order to consider different reflection models from approximately deterministic specular-type reflections to rough surface Lambertian reflections. The uncertainty in the source position is controlled by the parameter σ_0. Recall from Section 3.3 that we consider a disc $D_R \subset \Omega$ with centre $\boldsymbol{r}_0^*$ and radius R over which we model an uncertain location of the source point. In the example here we take $R = 0.05$.

Fig. 10 shows the numerical results for the interior density ρ_Ω for four combinations of σ_p and σ_0. The top-left sub-plot shows the case when $\sigma_p = \sigma_0 = 0.01$, which indicates a close to deterministic model for the location of the source point with approximately specular reflections. The bottom-right sub-plot shows the case when $\sigma_p = \sigma_0 = 10$, which indicates rough surface Lambertian reflections and a randomly located source point within the disc D_R. The other sub-plots show the two other different possible combinations of these parameter values.
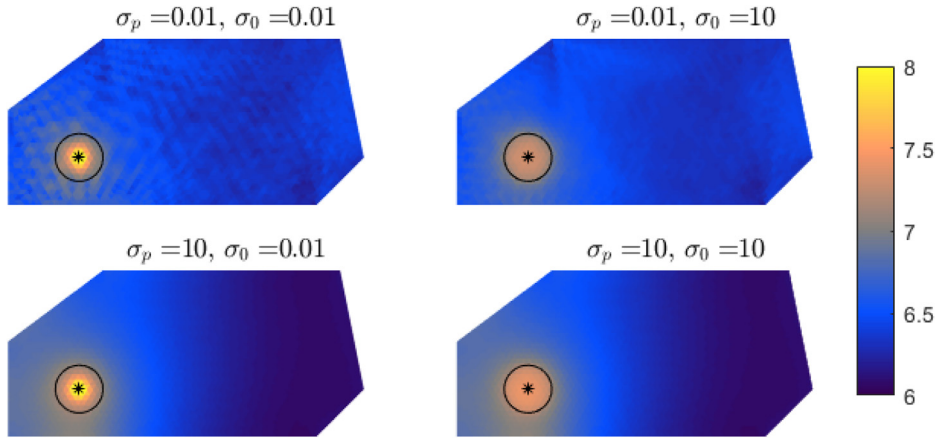
Fig. 10. Uncertain source point and rough boundary reflection simulation for four pairs of σ_p and σ_0 values. The plot shows the logarithm of the stationary interior density with mean source point position (0.15,0.1) indicated by a black dot and the boundary of the uncertain source region D_R indicated by a black circle. Parameter values: $c = 1$, $\sigma_s = 0$, $R = 0.05$, $\mu = 1$, $h = \sqrt{2}/60$ and $N = 128$.

In the left column of Fig. 10 one can clearly notice the effect of an approximately deterministic location for the source point with a sharp peak at $\mathbf{r}_0^* = (0.15, 0.1)$. This is similar to the behaviour observed in the left column of Fig. 9, where the simulations were performed with a deterministic point source. On the contrary, the right plots of Fig. 10 demonstrate results with a highly uncertain source point location within the disc D_R. It is evident that the source is equally spread across the whole disc D_R. The top row of Fig. 10 shows results with approximately specular reflections at the boundaries due to taking $\sigma_p = 0.01$. The top-left plot of Fig. 10 shows a strongly directive density distribution owing to the near deterministic nature of the source location and the approximately specular reflections. The behaviour is similar to that shown in the top-left plot of Fig. 9. An increase in the uncertainty of the source point location reduces this strong directivity and smoothes out the density distribution as can be observed in the top-right plot of Fig. 10. The lower two sub-plots of Fig. 10 are indistinguishable away from the source region D_R. Comparing the upper and lower rows of Fig. 10 shows that an approximately Lambertian reflection leads to less energy being transported to the right side of the domain due to the early reflections of the source density at the left side of the domain no longer being channelled to the right, but instead spreading more evenly throughout the polygon.

5. Conclusions

The modelling of parametric uncertainties within a boundary integral operator framework for transporting ray densities in finite two-dimensional domains has been discussed. In particular, we have derived explicit expressions for modelling a normally distributed stochastic perturbation of the propagation speed in the weak noise regime. In addition, we have described how the methodology may be extended to alternative models for the material parameter noise, whereby the uncertainty model would not be explicitly derived, but instead be based on a numerically interpolated PDF. We have also considered the modelling of geometric uncertainties in terms of both the location of an edge within a polygonal domain, and rough boundary reflections due to small scale geometric fluctuations. Uncertain source terms were also described, including stochastically distributed point sources and uncertain boundary data. Finally, we detailed the discretisation procedures employed, and then applied them to perform illustrative numerical examples for each of the uncertainty models described above. The results for an uncertain speed of propagation demonstrated the increasing likliehood of curved trajectory paths as the variance of the stochastic perturbation in the speed is increased, and a corresponding spreading of the tangential slowness. In addition, the results for both an uncertain boundary location and an uncertain source point location exhibit a smoothing effect on the interior density distribution. Finally, the incorporation of rough boundary reflections leads to a more diffusive solution for the interior density distribution resulting in a faster decay of the density across the domain due to an absence of directive ray transport.

Acknowledgement

Appendix A. Nonlinear trajectories arising from a linear perturbation of the propagation speed

In this appendix we detail an analytical solution of the dynamical system (12) with a linear propagation speed (16) for the special case when $\epsilon := \epsilon_x = \epsilon_y$. Note that analytical solutions for a number of choices of propagation speed, including

linear, can be found in Ref. [18]. For the case of a linear propagation speed (16) and with $\epsilon := \epsilon_x = \epsilon_y$, then the system (12) reduces to

$$\dot{\boldsymbol{r}} = c(\boldsymbol{r})^2 \boldsymbol{p},$$
$$c(\boldsymbol{r})\dot{\boldsymbol{p}} = -\epsilon \mathbf{1}, \tag{A.1}$$

where $\mathbf{1}$ is a vector of ones. To solve the system analytically we make use of the fact that (16) and (A.1) can be combined to give

$$\frac{\mathrm{d}}{\mathrm{d}t}(c(\boldsymbol{r})\boldsymbol{p}) = \epsilon((\mathbf{1}\cdot c(\boldsymbol{r})\boldsymbol{p})c(\boldsymbol{r})\boldsymbol{p} - \mathbf{1}), \tag{A.2}$$

which motivates the introduction of a new unknown $\boldsymbol{q} = c(\boldsymbol{r})\boldsymbol{p}$. Hence rescaling time via $\tau = \epsilon t$ leads to a new equation

$$\frac{\mathrm{d}}{\mathrm{d}\tau}\boldsymbol{q} = (\mathbf{1}\cdot\boldsymbol{q})\boldsymbol{q} - \mathbf{1}. \tag{A.3}$$

We now rewrite the system (A.1) with respect to the variables q^+ and q^- defined by

$$\begin{pmatrix} q^+ \\ q^- \end{pmatrix} := \begin{pmatrix} 1 & 1 \\ 1 & -1 \end{pmatrix}\boldsymbol{q} = A\boldsymbol{q}. \tag{A.4}$$

In these new variables, the system (A.3) can be expressed as

$$\frac{\mathrm{d}q^+}{\mathrm{d}\tau} = q^{+2} - 2 \quad \text{and} \quad \frac{\mathrm{d}q^-}{\mathrm{d}\tau} = q^+ q^-, \tag{A.5}$$

which is separable and can be solved analytically. For brevity we consider the case when the initial condition in the momentum variable is given by $\boldsymbol{p}_0 = (1, 0)^T$, however we note that the system (A.1) is rotationally invariant and so this choice is made without loss of generality. This gives the initial conditions for the system (A.5) as $q^+(0) = q^-(0) = 1$ and eventually we arrive at a solution for $\boldsymbol{q} = A^{-1}(q^+, q^-)^T = A(q^+/2, q^-/2)^T$ given by

$$\boldsymbol{q}(t) = \begin{pmatrix} \dfrac{\left(\mathrm{e}^{\sqrt{2}\epsilon t} + 1\right)\left((4 - 3\sqrt{2})\mathrm{e}^{\sqrt{2}\epsilon t} + \sqrt{2}\right)}{(6 - 4\sqrt{2})\mathrm{e}^{2\sqrt{2}\epsilon t} + 2} \\[4mm] \dfrac{\left(\mathrm{e}^{\sqrt{2}\epsilon t} - 1\right)\left((4 - 3\sqrt{2})\mathrm{e}^{\sqrt{2}\epsilon t} - \sqrt{2}\right)}{(6 - 4\sqrt{2})\mathrm{e}^{2\sqrt{2}\epsilon t} + 2} \end{pmatrix}. \tag{A.6}$$

The trajectory position coordinate $\boldsymbol{r}(t)$ may then be determined from $\boldsymbol{q}$ since $\dot{\boldsymbol{r}} = c(\boldsymbol{r})\boldsymbol{q}$. We can now solve this dynamical system using similar techniques by setting $(r^+, r^-)^T = A\boldsymbol{r}$, $(r_0^+, r_0^-)^T = A\boldsymbol{r}_0$ and then solving the transformed system

$$\dot{r^+} = (c_0 + \epsilon(r^+ - r_0^+))q^+,$$
$$\dot{r^-} = (c_0 + \epsilon(r^+ - r_0^+))q^-. \tag{A.7}$$

For brevity of notation, but without loss of generality, we give only the solution with the initial condition $\boldsymbol{r}_0 = \mathbf{0}$:

$$r_x(t) = \frac{c_0(\mathrm{e}^{\sqrt{2}\epsilon t} - 1)(29\sqrt{2} + 41 + (7 + 5\sqrt{2})(\mathrm{e}^{\sqrt{2}\epsilon t} + \mathrm{e}^{2\sqrt{2}\epsilon t}) + (1 + \sqrt{2})\mathrm{e}^{3\sqrt{2}\epsilon t})}{\epsilon(58 + 41\sqrt{2} + (14\sqrt{2} + 20)\mathrm{e}^{2\sqrt{2}\epsilon t} + (2 + \sqrt{2})\mathrm{e}^{4\sqrt{2}\epsilon t})},$$
$$r_y(t) = -\frac{c_0(\mathrm{e}^{\sqrt{2}\epsilon t} - 1)^2(12\sqrt{2} + 17 + (2\sqrt{2} + 3)\mathrm{e}^{2\sqrt{2}\epsilon t})}{\epsilon(58 + 41\sqrt{2} + (14\sqrt{2} + 20)\mathrm{e}^{2\sqrt{2}\epsilon t} + (2 + \sqrt{2})\mathrm{e}^{4\sqrt{2}\epsilon t})}. \tag{A.8}$$

Considering Taylor expansions of the exponential terms in (A.8) close to $\epsilon = 0$, one can show that the solution converges to straight line trajectories given by $r_x(t) = c_0 t$ and $r_y(t) = 0$ as $\epsilon \to 0$.

Supplementary material

Supplementary material associated with this article can be found, in the online version, at 10.1016/j.cnsns.2019.104973.

References

[1] Cvitanović P, Dettmann CP, Mainieri R, Vattay G. Trace formulas for stochastic evolution operators: weak noise perturbation theory. J Stat Phys 1998;93:981–99.
[2] Cvitanović P, Artuso R, Mainieri R, Tanner G, Vattay G. Chaos: classical and quantum. Copenhagen: Niels Bohr Institute; 2012. ChaosBook.org
[3] Cvitanović P, Lippolis D. Knowing when to stop: how noise frees us from determinism. In: Robnik M, Romanovski VG, editors. Let's face chaos through nonlinear dynamics, Melville, New York: Am. Inst. of Phys.; 2012. p. 82–126.
[4] Chappell DJ, Tanner G. A boundary integral formalism for stochastic ray tracing in billiards. Chaos 2014;24:043137.
[5] Sinai YG. What is a billiard? Not Am Math Soc 2004;51:412–13.

[6] Froyland G, Junge O, Koltai P. Estimating long term behavior of flows without trajectory integration: the infinitesimal generator approach. SIAM J Num Anal 2013;51(1):223–47.

[7] Risken H. The Fokker–Planck equation. New York: Springer; 1996.

[8] Cvitanović P, Dettmann CP, Mainieri R, Vattay G. Trace formulas for stochastic evolution operators: smooth conjugation method. Nonlinearity 1999;12:939–53.

[9] Cvitanović P, Søndergaard N, Palla G, Vattay G, Dettmann CP. Spectrum of stochastic evolution operators: local matrix representation approach. Phys Rev E 1999;60:3936–41.

[10] Palla G, Vattay G, Voros A, Søndergaard N, Dettmann CP. Noise corrections to stochastic trace formulas. Found Phys 2001;31:641–57.

[11] Lippolis D, Cvitanović P. How well can one resolve the state space of a chaotic map? Phys Rev Lett 2010;104:014101.

[12] Heninger JM, Lippolis D, Cvitanović P. Neighborhoods of periodic orbits and the stationary distribution of a noisy chaotic system. Phys Rev E 2015;92:062922.

[13] Ulam S. Problems in modern mathematics. New York: John Wiley & Sons; 1964.

[14] Bollt E, Gora P, Ostruszka A, Zyczkowski K. Basis Markov partitions and transition matrices for stochastic systems. SIAM J Appl Dyn Sys 2008;7(2):341–60.

[15] Heninger JM, Lippolis D, Cvitanović P. Perturbation theory for the Fokker–Planck operator in chaos. Commun Nonlinear Sci Numer Simulat 2018;55:16–28.

[16] Chappell DJ, Tanner G. Uncertainty quantification for phase-space boundary integral models of ray propagation. Wave Motion 2019;87:151–65.

[17] Chappell DJ. Tanner g. solving the liouville equation via a boundary element method. J Comp Phys 2013;234:487–98.

[18] Červený V. Seismic ray theory. Cambridge: Cambridge University Press; 2001.

[19] Koskela J, Vahala E, de Greef M, Lafitte LP, Ries M. Stochastic ray tracing for simulation of high intensity focal ultrasound therapy. J Acoust Soc Amer 2014;136:1430–40.

[20] Vorlander M, Mommertz E. Definition and measurement of random-incidence scattering coefficients. Applied Acoustics 2000;60:187–99.

[21] Haarscher A, De Doncker P, Lautru D. Uncertainty propagation and sensitivity analysis in ray tracing simulations. Progress Electromagnet Res M 2011;21:149–61.

[22] Imbeaux F, Peysson Y. Ray-tracing and Fokker–Planck modelling of the effect of plasma current on the propagation and absorption of lower hybrid waves. Plasma Phys Control Fusion 2005;47:2041–65.

[23] Lyon RH. Statistical analysis of power injection and response in structures and rooms. J Acoust Soc Am 1969;45:545–65.

[24] Lyon RH, DeJong RG. Theory and application of statistical energy analysis. 2nd ed. Boston: Butterworth-Heinemann; 1995.

[25] Reynders E, Legault J, Langley RS. An efficient probabilistic approach to vibro-acoustic analysis based on the gaussian orthogonal ensemble. J Acoust Soc Amer 2014;136:201–12.

[26] Gradoni G, J-H Y, Xiao B, Antonsen TM, Anlage SM, Ott E. Predicting the statistics of wave transport through chaotic cavities by the random coupling model: a review and recent progress. Wave Motion 2014;51(4):606–21.

[27] Bajars J, Chappell DJ. A boundary integral method for modelling vibroacoustic energy distributions in uncertain built up structures. J Comp Phys 2018;373:130–47.

[28] Mun J. Advanced analytical models: over 800 models and 300 applications from the basel ii accord to wall street and beyond. Hoboken: John Wiley and Sons; 2008.

[29] Phong BT. Illumination for computer generated pictures. Commun ACM 1975;18(6):311–17.

[30] Bajars J, Chappell DJ, Hartmann T, Tanner G. Improved approximation of phase-space densities on triangulated domains using discrete flow mapping with p-refinement. J Sci Comp 2017;72:1290–312.

[31] Boyd JP. Chebyshev and Fourier spectral methods. 2nd ed. Mineola, New York: Dover; 2000.